



Effects of cloud vertical structure on the development of tropical cyclones: A case study based on In-Fa (2021)



Enwang Luo ^a, Guoxing Chen ^{a,b,*}, Wei-Chyung Wang ^c, Jie Feng ^a, Yanhong Gao ^a

^a Department of Atmospheric and Oceanic Sciences, Institute of Atmospheric Sciences, and CMA-FDU Joint Laboratory of Marine Meteorology, Fudan University, Shanghai, China

^b Shanghai Frontiers Science Center of Atmosphere-Ocean Interaction, Fudan University, Shanghai, China

^c Atmospheric Sciences Research Center, University at Albany, State University of New York, Albany, NY, USA

ARTICLE INFO

Keywords:

Tropical cyclone
Cloud vertical structure
Machine learning
Cloud fraction parameterization

ABSTRACT

This study conducted WRF simulations of Typhoon In-Fa (2021), which caused significant damage to the eastern China in 2021, to investigate how cloud vertical structure may affect the development of a tropical cyclone (TC). Specifically, the TC was simulated using two cloud-fraction schemes: the default Xu-Randall (XR) scheme and a newly-developed neural Network-based Scale-Adaptive (NSA) scheme. Results show that the NSA scheme simulates a more eastward TC track than the XR scheme for both the pre-landfall and landfall phases and is closer to the observation. The underlying mechanisms differ between the two phases and are closely associated with the TC asymmetric structure and phase evolution. First, the XR scheme simulates larger cloud fractions than the NSA scheme across the entire TC, yielding a stronger longwave cloud radiative effect (LWCRE). This tends to increase the instability and invigorates the convection. Second, the relatively strong convective in the northeast quadrant of the TC cause a horizontally-distributed cloud layer, where the NSA scheme simulates a less-tilted cloud structure and a more pronounced horizontal gradient of LWCRE, which can amplify the secondary circulation.

During the pre-landfall phase, the effects of increased instability and enhanced secondary circulation in the northeast quadrant tend to counterbalance each other, making the instability effect in the southwest quadrant dominate changes of the TC track. This increases the cloud ice water path (IWP) and latent heating in the west of the TC in the XR simulation, shifting the TC track westward. During the landfall phase, cloud fraction decreases throughout the TC, diminishing the instability effect and allowing the secondary circulation effect in the northeast quadrant to become dominant. This increases the IWP and latent heating in the east of the TC in the NSA simulation, shifting the TC track eastward.

1. Introduction

Tropical cyclones (TC) are among the most destructive natural disasters on Earth, posing significant threats to the safety of human lives and properties. In the coastal areas of China, TC caused 12 fatalities (missing) and a direct economic loss of 47.5 billion CNY in 2023 (<https://news.cctv.com>), heading the list of various natural disasters. However, the prediction of TC genesis and development is still difficult due to inadequate understanding of relevant physical processes (e.g., Yang et al., 2022).

Many factors may affect the TC genesis and development, such as the vertical wind shear (Reasor et al., 2013; DeHart et al., 2014) and the

asymmetric factor (e.g., the wind field asymmetry; Ueno, 2007; Olfateh et al., 2017; Wen et al., 2019). In recent years, the radiation processes are increasingly shown to play important roles throughout the TC lifetime (e.g., Nicholls, 2015; Ruppert Jr. et al., 2020; Yang et al., 2022; Xu and Takemi, 2022). First, the large-scale environmental cooling increases humidity, aiding condensation and enhancing atmospheric destabilization (Miller and Frank, 1993; Fu et al., 1995; Dudhia, 1989; Tao et al., 1996). Second, the differential radiative heating between cloudy areas within TC and clear-sky areas outside TC creates warming anomalies within the storm and cooling anomalies in the surroundings, driving secondary circulations that favor TC development (Gray and Jacobson, 1977; Craig, 1996; Nicholls, 2015; Muller and Romps, 2018).

* Corresponding author at: Department of Atmospheric and Oceanic Sciences, Institute of Atmospheric Sciences, and CMA-FDU Joint Laboratory of Marine Meteorology, Fudan University, Shanghai, China.

E-mail address: chengguoxing@fudan.edu.cn (G. Chen).

Third, the radiative destabilization, characterized by cooling at cloud tops and warming at cloud bases, promotes deep convection, especially at night (Webster and Stephens, 1980; Hobgood, 1986; Xu and Randall, 1995; Tang et al., 2019). Evidently, clouds are crucial to the TC-radiation interactions, suggesting the importance of realistic simulations of clouds and related cloud radiative effects (CREs) to accurate TC predictions (Houze, 2010).

However, the representation of clouds and their CREs is still challenging to numerical models. On the one hand, the limit of computational resources hinders models from applying more correct but computationally expensive parameterizations for certain well-understood processes (e.g., the bin cloud micro-physical parameterization; Khain et al., 2005). On the other hand, and worse still, some key processes, such as sub-grid scale physics (Seinfeld et al., 2016), remain poorly understood, which hampers the ability to parameterize them accurately. For example, the cloud fraction, which is a sub-grid property for most models and affects both shortwave (SW) and longwave (LW) CREs, is difficult to be parameterized because of inadequate understanding of the sub-grid variations of temperature, humidity, vertical velocity, and their correlations (Wang et al., 2015, 2022). The study by Wang et al. (2023) showed that two frequently-used cloud-fraction parameterization schemes, the XR scheme (Xu and Randall, 1996) and the Sundqvist scheme (Sundqvist et al., 1989), both tended to overestimate the high-level cloud fractions at the tropics but underestimate the low- and mid-level cloud fractions near 60° of both hemispheres.

Recently, we have developed a neural Network-based Scale-Adaptive (NSA) cloud-fraction scheme (Chen et al., 2023). The offline evaluation showed that when given the observed grid-mean cloud water contents and relative humidity, the NSA scheme can greatly improve the cloud-fraction simulation in terms of both spatial distribution and vertical structure compared with the conventional XR scheme. As the high- and low-level clouds differ greatly in SWCRE and LWCRE, it is intuitive to infer that employing this new scheme may place an impact on TC simulations.

Therefore, this study is aimed to investigate the impacts of the NSA scheme on TC simulations. Specifically, it addresses three questions: 1) To what extent does the NSA cloud-fraction scheme modify the cloud vertical structure (CVS) in a TC simulation compared to the conventional XR scheme? 2) How might these modifications subsequently influence the TC development? And 3) what are the mechanisms that link the CVS changes to the TC development? The study was carried out based on WRF (Weather Research and Forecast) model simulations of the Typhoon In-Fa (2021), which caused record-breaking rainfall, extensive flooding, and power outages in eastern China in 2021, compelling the highest (level 1) emergency response for natural disaster relief be initiated (Wu et al., 2022).

The rest of this manuscript is arranged as follows: Section 2 describes the two cloud fraction parameterization schemes (i.e., XR and NSA schemes) and the experimental setup; Section 3 presents the effects of the cloud-fraction scheme on simulated cloud properties and the TC development; Section 4 examines the underlying mechanisms by which the CVS affects the TC development; Section 5 discusses issues relevant to the result sensitivities; and the conclusions are given in Section 6.

2. Method

2.1. XR and NSA cloud-fraction parameterization schemes

The XR and NSA cloud-fraction schemes are both diagnostic schemes, which assume the sub-grid cloud fraction (CF) to be a function of instantaneous grid-mean atmospheric properties, such as cloud water contents and relative humidity. These two schemes were fully described in Xu and Randall (1996) and Chen et al. (2023), respectively. Interested readers are referred to these papers for details of the two schemes, whereas a brief introduction is given below.

The XR scheme calculates CF using the following equations:

$$C_s = R^\beta \left[1 - \exp \left(- \frac{\alpha Q_c}{[(1-R)Q^*]^\gamma} \right) \right], R < 1 \quad (1)$$

$$C_s = 1, R \geq 1 \quad (2)$$

where R , Q_c , Q^* indicate the grid-mean relative humidity, cloud condensate mixing ratio (i.e., the sum of liquid and ice cloud mixing ratios), and saturated water vapor mixing ratio, respectively, and $\alpha = 100$, $\beta = 0.25$, and $\gamma = 0.49$ are empirical parameters determined via curve-fitting based on simulation data of a cloud ensemble model.

Clearly, the XR scheme has a simple form and is easy to implement in models. It is the default cloud-fraction scheme in the WRF model and was used in many WRF-based studies (e.g., Chen and Wang, 2016; Chen et al., 2018, 2021; Song et al., 2019; Yang et al., 2018). This scheme has been shown to have superiorities over the Sundqvist scheme, another frequently-used scheme in the WRF model (Wang et al., 2023). Thus, this study takes the XR scheme as representative of conventional cloud-fraction schemes and a reference for assessing the impact brought by the NSA scheme.

In contrast, the NSA scheme does not have an explicit formula form. Instead, it calculates the sub-grid CF using a multiple-layer perceptron neural network, where the network parameters were determined via training based on CloudSat observational datasets. The network inputs include the grid-mean air pressure, air temperature, cloud liquid/ice water mixing ratios, relative humidity over ice/water surfaces (similar to inputs of the XR scheme) as well as the horizontal and vertical grid sizes to account for effects of grid sizes on the sub-grid CF.

Compared with conventional cloud-fraction schemes, the NSA scheme has three distinctive features. First, it leverages neural networks and thus avoids the need for potentially improper assumptions about the form of parameterization formulas and the sub-grid statistics. Second, its development was based on the CloudSat data, which allows it to better align with observations compared to schemes derived from simulation data. Third, it accounts for the impacts of both horizontal and vertical resolutions on cloud-fraction parameterization. Offline evaluations have demonstrated that the NSA scheme surpasses the XR scheme when provided with observed grid-mean properties (Chen et al., 2023). Furthermore, our recent study (Li et al., 2024) revealed that employing the NSA scheme in regional climate simulations of the Tibet Plateau yields larger mid-level and high-level cloud fractions and stronger LWCRE relative to using the XR scheme, which warms the surface and significantly mitigates winter surface temperature cold biases by up to 4 °C (approximately 50 % of the total biases).

2.2. Experiment setup

This study used the WRF model version 4.4 to simulate the Typhoon In-Fa (2021). This typhoon formed as a tropical storm in the western north Pacific on 17 July 2021, made the first landfall in Zhejiang on 25 July 2021 and a second landfall in Shanghai on 26 July 2021, and moved northward to Jiangsu afterward. Before landfall, it enhanced atmospheric moisture transport to Henan Province, contributing to the unprecedented heavy rainfall there (Nie and Sun, 2022); and after landfall, it stayed in the continent for nearly 95 h, setting a record for the longest residence time and causing record-breaking rainfall at many stations in Zhejiang, Shanghai, and Jiangsu (Wu et al., 2022).

Fig. 1 presents the simulation domain setup. Two two-way nested domains were used. The outer domain consists of 120 × 100 grids with a horizontal resolution of 27 km while the inner domain consists of 202 × 181 grids with a horizontal resolution of 9 km. Vertically there are 50 layers with the model top at 50 hPa.

Two cases were simulated. The two cases differ only in the cloud-fraction scheme: one used the XR scheme while the other used the NSA scheme. Hereafter, the two cases were termed as XR and NSA, respectively. Other physics parameterizations were configured as follows: the Thompson scheme (Thompson et al., 2004) for cloud

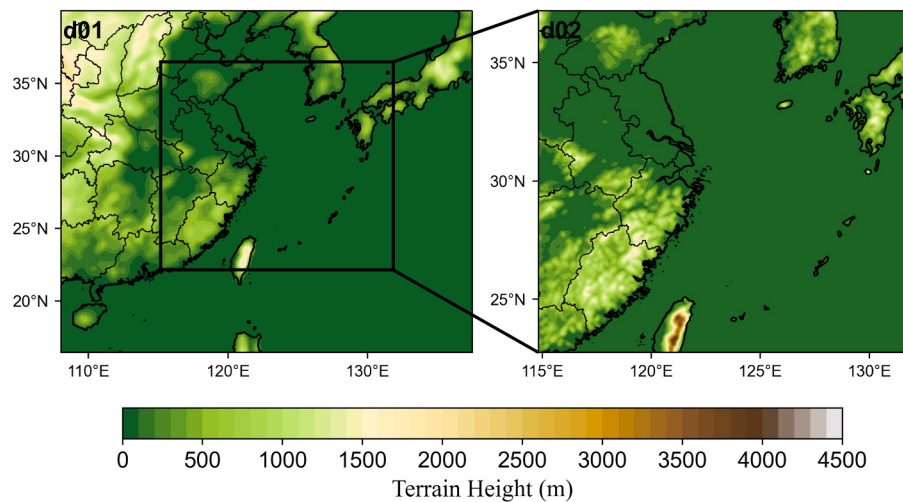


Fig. 1. WRF domain setup. The outer domain consists of 120×100 grids with a resolution of 27 km, and the inner domain consists of 202×181 grids with a resolution of 9 km. Shadings indicate the surface terrain height.

microphysical physics, the RRTMG schemes (Iacono et al., 2008) for shortwave and longwave radiation transfer, the MYJ scheme (Janjić, 1994) for boundary-layer physics, the revised Monin-Obukhov scheme (Hong et al., 2006) for surface layer physics, and the Tiedtke scheme for cumulus convention (Tiedtke, 1989; Zhang et al., 2011). The initial fields and boundary forcings were both from the Final Global Analysis $1^\circ \times 1^\circ$ reanalysis (NCEP/FNL, <https://rda.ucar.edu/datasets/ds083.2>).

The simulation of both cases spanned 5 days (0000 UTC 22 July–0000 27 July 2021). The first day was discarded as the model spin-up period. During this period, the spectral nudging was applied in d01 to improve the simulation accuracy in both simulations, where a wave number of 3 was set in both directions. The following four analysis days were divided into three phases: a pre-landfall phase (0000 UTC 23

July–0000 25 July 2021), a landfall phase (0000 UTC 25 July–0000 26 July 2021), and a post-landfall phase (0000 UTC 26 July–0000 27 July 2021). The simulation data were stored every 3 h.

3. Effects of cloud-fraction schemes on the TC simulation

In this section, we first examine the differences in simulated cloud properties between the XR and NSA cases, and then examine their caused changes in the simulated TC track and intensity.

3.1. Comparison of simulated cloud properties

Fig. 2 compares the cloud liquid water path (LWP), ice water path

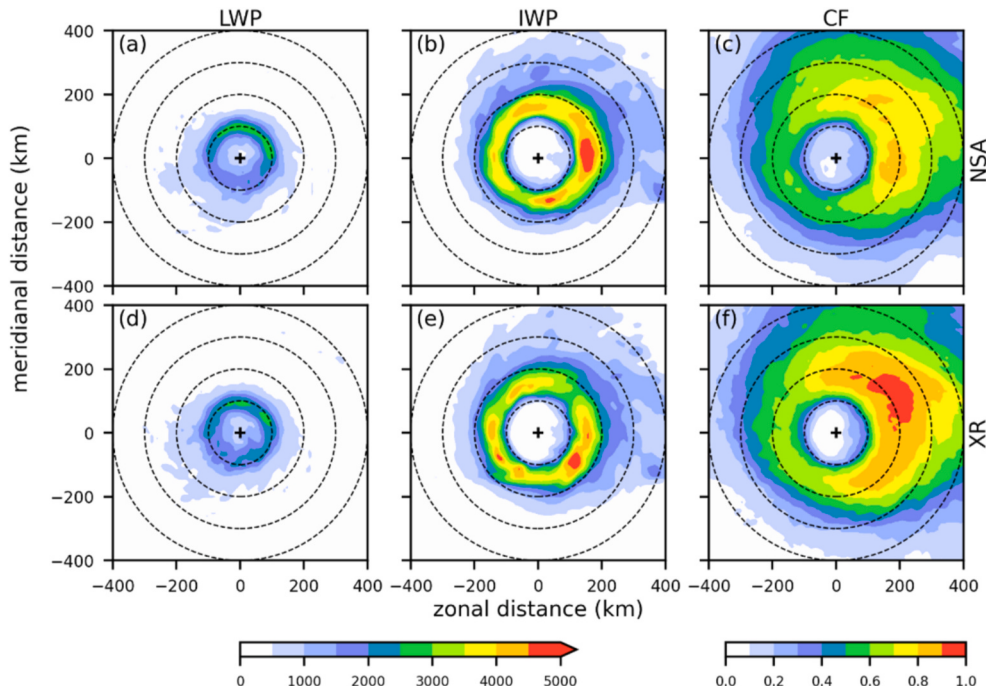


Fig. 2. The plain views of cloud liquid water path (LWP; units: g m^{-2}), ice water path (IWP; units: g m^{-2}) and total cloud fraction (CF) from NSA (a–c) and XR (d–f) simulations, averaged over the period of 0000 UTC 23 July to 0000 UTC 27 July 2021 for the range of 400 km from the TC center (plus signs). The dashed circles denote the positions at distances of 100, 200, 300, and 400 km from the TC center. The total cloud fraction was calculated assuming maximum-random overlap. Note that IWP was calculated as the vertical integration of cloud ice and snow masses to be consistent with the radiation calculation.

(IWP), and total cloud fraction (CF) from the NSA and XR simulations, averaged throughout 0000 UTC 23 July–0000 UTC 27 July for the range of 400 km from the TC center. The LWP and IWP in the NSA simulation (Figs. 2a–b) both exhibit a prominent ring structure with high values concentrated in the range of 100–200 km to the center. LWP is much smaller than IWP and with maximums located closer to the TC center, in line with the slanted CVS shown below. The CF also presents a ring-like pattern and clearly is larger in the east than in the west.

The general patterns of LWP, IWP, and CF from the XR simulation closely resemble those obtained from the NSA simulation (Figs. 2d–f). However, notable differences exist. First, the NSA simulation exhibits more extensive regions with LWP exceeding 1000 g m^{-2} and IWP surpassing 5000 g m^{-2} compared to the XR simulation. Second, IWP in the east is larger in NSA than in XR while that in the west is larger in XR. Given that IWP dominates LWP in both simulations, it can be inferred that the NSA simulation displays stronger convection in the eastern part of the TC and weaker convection in the western part relative to the XR simulation. Thirdly, the NSA simulation shows a smaller cloud fraction across most areas compared to the XR simulation.

Fig. 3 compares the vertical structures of cloud fraction as a function of radial distance in the two simulations. The NSA simulation exhibits two distinct peaks: one at approximately 750–700 hPa and the other at 300–200 hPa. In contrast, the XR simulation also displays two peaks, but with notably higher cloud fractions at most vertical levels and radial distances. The vertical and radial extents of both peaks are considerably larger in the XR simulation. Particularly, the low-level cloud fraction in the XR simulation extends significantly farther outward than in the NSA simulation.

To understand the cloud-fraction differences, we analyze how cloud fraction varies with the grid-mean relative humidity (R) and cloud condensate mixing ratio (Q_c) across two simulations. As shown in Fig. 4, two features stand out. First, the WRF model tends to simulate very small values of Q_c for all three cloud phases (i.e., ice, mixed, and liquid phases) in the two simulations when the grid is sub-saturated (indicated by the probability density contours). These patterns are quite different from the CloudSat observational results shown in Wang et al. (2023) and Chen et al. (2023). Second, the NSA scheme generally predicts a larger cloud fraction than the XR scheme under the conditions where the grid is subsaturated ($R < 1$) and the cloud condensate mixing ratio is relatively small ($Q_c < 250 \text{ mg kg}^{-1}$ for ice-only clouds, $Q_c < 200 \text{ mg kg}^{-1}$ for mixed-phase clouds, and $Q_c < 1000 \text{ mg kg}^{-1}$ for liquid-only cloud). Conversely, in other situations (e.g., $R > 1$), the NSA scheme predicts a smaller cloud fraction (Fig. 4c, f, and i). Given that cloudy grids ($Q_c > 0$) are dominated by high R in both simulations, the NSA simulation

exhibits smaller cloud fractions in most situations, which is shown above in Fig. 3.

3.2. Track and intensity

Fig. 5 presents the TC track, the maximum 10-m wind speed near the TC center, and the central pressure from the NSA and XR simulations, compared with the best estimate by the Joint Typhoon Warning Center (JTWC). Both simulations generally reproduce the temporal evolution of the TC location and intensity throughout the analysis period. The TC track from the NSA simulation is notably closer to the observations than that from the XR simulation (Fig. 5a). The accumulated track error in the NSA simulation is just half that in the XR simulation. Particularly, the two landfall locations in the NSA simulation nearly match the observed locations. In contrast, the TC track in the XR simulation is shifted westward relative to the observations. While the NSA simulation also exhibits this westward bias, the bias is significantly reduced compared with the XR simulation.

The TC intensity is overestimated in both NSA and XR simulations, as evidenced by the larger maximum wind speeds near the TC center (Fig. 5b) and the lower central pressure (Fig. 5c). The two simulations show minimal differences before the first landfall (00 UTC on 25 July). After the first landfall, the NSA simulation produces a slightly stronger TC than the XR simulation, indicating a slower weakening rate in the NSA case.

Overall, the NSA simulation produces distinct cloud properties compared with the XR simulation, indicating that the NSA and XR cases exhibit relatively stronger convection in the eastern and western parts of the TC, respectively. Consequently, the TC track in NSA is shifted eastward relative to that in the XR simulation, aligning more closely with observations. In contrast, the TC intensity does not show marked differences between two cases before the landfall, and is slightly stronger in the NSA case during the landfall. The following section delves into the detailed mechanisms through which the CVS influences the TC evolution.

4. Underlying mechanisms

Considering that the role of cloud radiative effects can vary during different stages of the TC development (e.g., Ruppert Jr. et al., 2020; Yang et al., 2022), we investigate the underlying mechanisms for the pre-landfall and landfall phases separately.

We have examined steering flows in the two simulations and found that the differences between them remain insignificant until 26 July (figure not shown). This suggests that the changes in steering flows have a limited impact on the changes in the TC track. In contrast, the beta-drift effect plays a more crucial role. As shown in Fig. 6, across four analysis days, the geopotential height at 500 hPa is notably higher in the western part and lower in the eastern part in the NSA simulation than that in the XR simulation. This asymmetric wave-number 1 structure tends to steer the TC northeasterward (Wu and Wang, 2000), consistent with the simulated changes in the TC track.

Furthermore, this asymmetric pattern aligns with the differences in the IWP (Fig. 2) and the TC track (Fig. 5). Specifically, the high anomalies in the west are more pronounced during the pre-landfall phase (23–24 July), whereas the low anomalies in the east become more prominent during the landfall phase (25 July). In addition, the relatively larger IWP in the west in the XR simulation and the relatively larger IWP in the east in the NSA simulation are also more distinct during the pre-landfall and landfall phases, respectively (figure not shown). Therefore, in the following analysis, we focus in the western part of the TC during the pre-landfall phase and in the eastern part during the landfall phase, respectively, to reveal detailed mechanisms that link changes in cloud fractions with changes in the TC track.

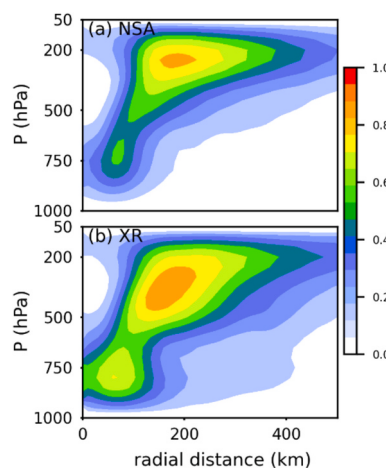


Fig. 3. Radial height cross-sections of cloud fraction from NSA (a) and XR (b) simulations, averaged over the period of 0000 UTC 23 July to 0000 UTC 27 July 2021.

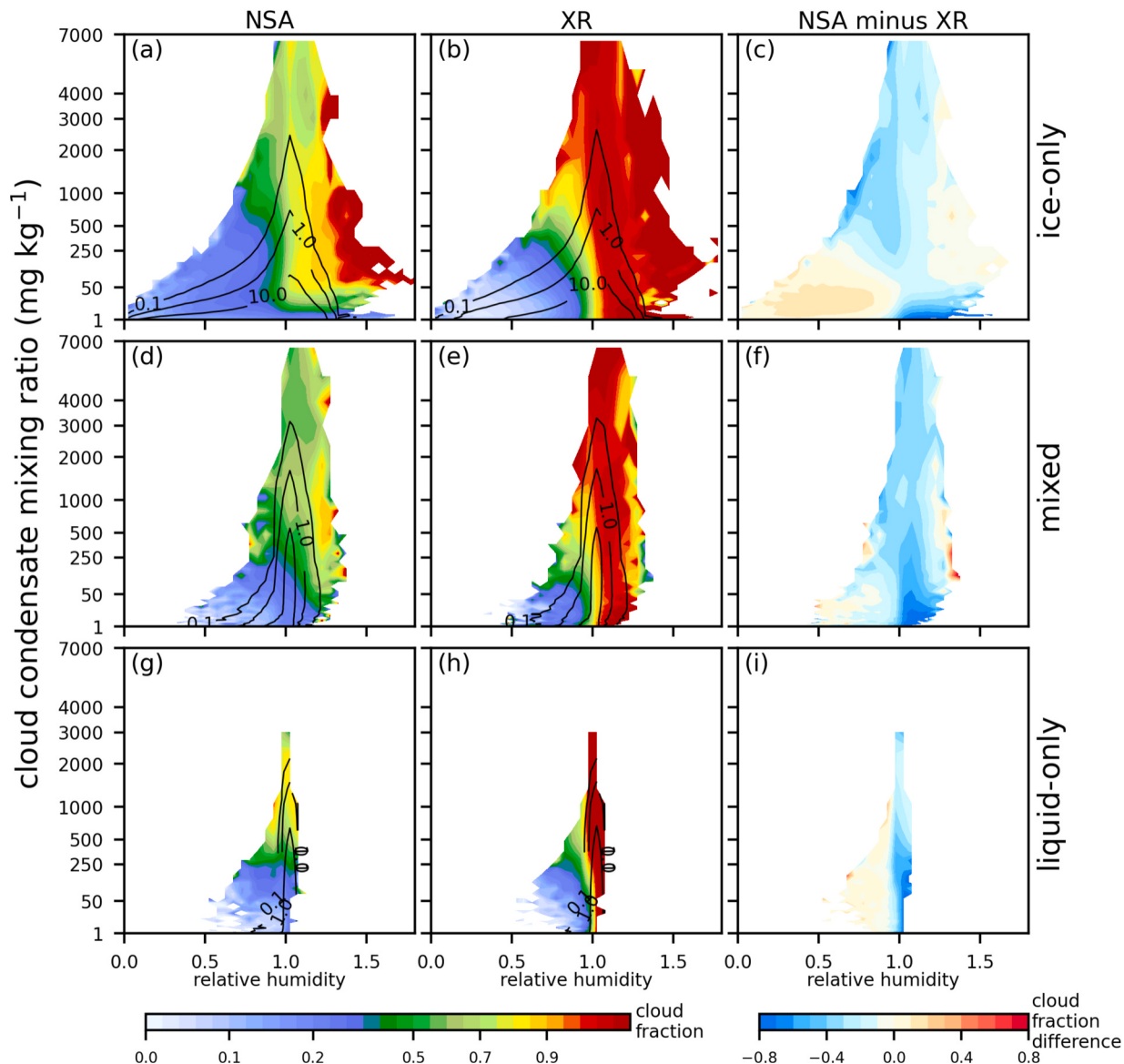


Fig. 4. Cloud fraction as a function of cloud condensate mixing ratios (Q_c) and relative humidity (R) from NSA (a, d, and g) and XR (b, e, and h) simulations and their differences (c, f, and i; NSA minus XR). The rows represent the cloud phase of ice-only, mixed, and liquid-only. Black lines indicate contours of the probability density of 0.1, 1, and 10. For both NSA and XR simulations, more than 95 % percent of samples lie below the 0.1 contour.

4.1. Pre-landfall phase

Here we mainly present results for the southwest quadrant of the TC, where the XR simulation exhibits a larger IWP than the NSA simulation. The findings of the northwest quadrant are quite similar (figure not shown).

Fig. 7 compares the vertical cross-sections of cloud fractions averaged in the southwest quadrant for the pre-landfall phase between the two simulations (Figs. 7a–b). In both simulations, the cloud fractions display features similar to those averaged over the entire analysis period (as shown in Fig. 3). The most notable differences between the simulations are found in the mid-upper troposphere, where the XR simulation shows larger cloud fractions, with a more extensive region where cloud fraction exceeds 0.8.

Previous studies showed that large volumes of eyewall clouds are highly effective at trapping the longwave radiation, which can warm the lower atmospheric levels and induce a second circulation that favors TC developments (Ruppert Jr. et al., 2020; Yang et al., 2021; Bu et al., 2014). Thus, we examine the longwave radiative heating rates of two

simulations in Figs. 7c–f. For the all-sky condition (LWHR-ALL; Figs. 7c–d), both simulations display strong warming in the cloudy eyewall (indicated by the dashed contours) and strong cooling within the eye. However, the eyewall warming and in-eye cooling in the XR simulation are notably stronger than those in the NSA simulations. For the clear-sky condition (LWHR-CLR; Figs. 7e–f), the two simulations show minimal differences. Both are characterized by cooling within the eyewall and weak warming around the cloud tops. Thus, it can be concluded that the LWHR differences between the two simulations are primarily due to the cloud differences rather than differences in water vapor contents or temperature profiles. Specifically, the higher cloud volumes in the XR simulation yield stronger heating within the high-altitude eyewall clouds and more pronounced cooling effects in the eye, compared to that in the NSA simulation.

The different LWHRs lead to differences in the TC thermodynamic structure. The stronger in-eye cooling in the XR simulation enhances the convective instability and intensifies the upward motion along the slanted eyewall (100–150 km from the TC center; Fig. 8a). This anomalous ascent motion, though gentle, is significant due to its large spatial

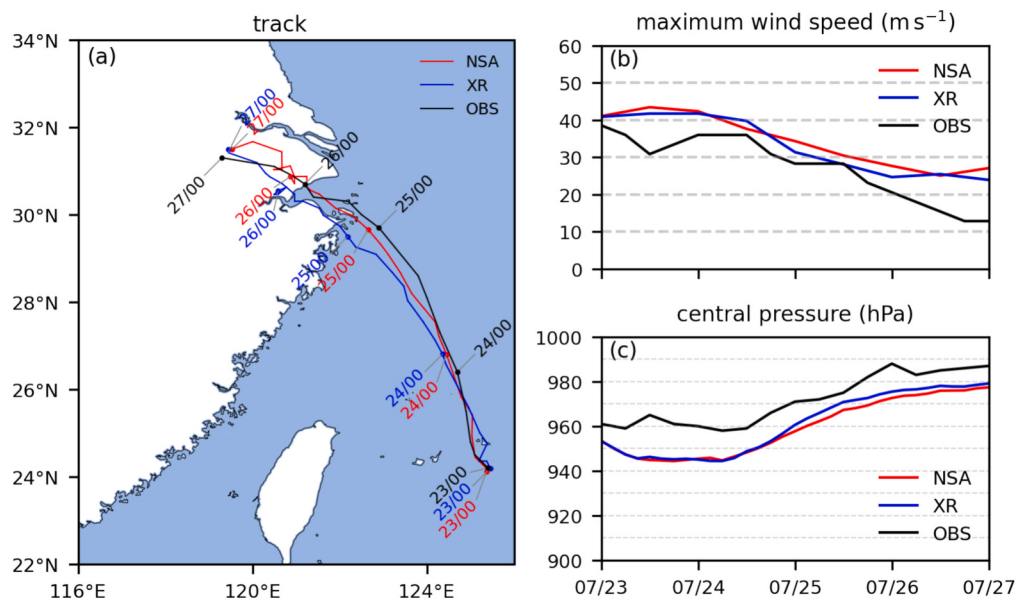


Fig. 5. WRF simulated TC tracks (a), maximum wind speeds at the 10-m height around the TC center (b), and the TC central pressures (c) from 0000 UTC 23 July to 0000 UTC 27 July 2021 in two simulations, as compared with the JTWC observations. The 6-hourly simulation data were used in the plot to match the observations. The accumulated track error (simple summation) throughout the pre-landfall and landfall period is 314 km for the NSA simulation and 625 km for the XR simulation.

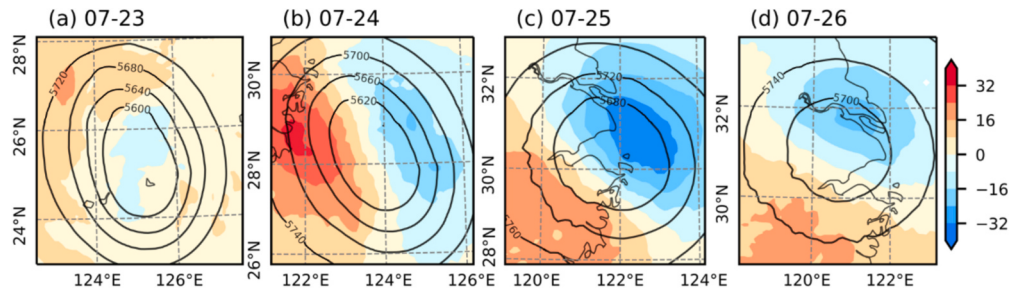


Fig. 6. Difference of 500-hPa geopotential height (unit: gpm) between NSA and XR simulations (shadings; NSA minus XR) at 1200 UTC of four analysis days. Black contours indicate geopotential heights from the NSA simulation to facilitate the result interpretation.

extent and long temporal persistence (Bu et al., 2014). As a result, more water vapor is transported upward by stronger updrafts, leading to increased deposition and condensation, and more latent heating at upper levels (Fig. 8b). This tends to further intensify the top-heavy radiative heating structure and yield a positive feedback mechanism (Yang and Tan, 2020). This process results in a lower geopotential height in the western part of the TC in the XR simulation and shifts the TC track more westward compared to the NSA simulation.

4.2. Landfall phase

During the landfall phase (0000 UTC 25 July–0000 UTC 26 July), the low anomalies of 500-hPa geopotential height in the NSA simulation are the most significant in the northeast quadrant of the TC (Fig. 6c). Thus, here we mainly present results over the northeast quadrant of the TC.

Fig. 9 compares the vertical cross-sections of cloud fractions and LWHRs averaged in the northeast quadrant for the landfall phase between the two simulations (Figs. 9a-f). Clearly, both the values of cloud fractions and the radial extent of the eyewall clouds are smaller in this phase than in the pre-landfall phase. Notably, cloud fractions exceeding 0.8 are only present in the upper levels of the NSA simulation, suggesting that the NSA simulation exhibits stronger convective activities than the XR simulation. Although the XR simulation still shows larger cloud fractions at most levels (which still tends to increase the instability in the XR simulation), the differences between the two simulations are

less pronounced than in the previous stage (Figs. 7a-b). The primary CVS differences are evident in the tilt of the eyewall clouds. Specifically, the XR simulation shows larger cloud fractions in the mid-upper troposphere (100–300 km, 500–350 hPa) and a greater radial extent with cloud fractions exceeding 0.5 in the upper levels (400–500 km, 300–150 hPa), indicating that the eyewall clouds in the XR expand more radially outward. We have quantified the degree of eyewall cloud tilt using the difference between the eyewall cloud radii at 700 hPa and 150 hPa (similar to the method in Yang et al., 2022) and found it to be 70 km for the NSA simulation and 150 km for the XR simulation.

The difference in eyewall cloud tilt between the two simulations can be attributed to stronger LWCRe in the XR simulation (Figs. 7c-d) associated with its relatively larger cloud fraction in the XR simulation (Fig. 3, and Figs. 7a-b). The strong LWCRe stimulates stronger convective activities (as discussed in Section 4.1), leading to stronger outflows in the upper levels and enhanced radiative heating on the outer side of the eyewall. This subsequently results in a more tilted eyewall (Bu et al., 2014; Fovell et al., 2016; Yang et al., 2022).

Because of the differences in eyewall cloud tilt, the LWHR-ALL exhibits a vertically extending shape throughout the troposphere in the NSA simulation, whereas it is almost horizontally extended in the XR simulation (Fig. 9c-d). This results in a larger radial gradient of the LWHR-ALL in the NSA simulation, which causes secondary circulations to enhance the moisture and momentum transport towards the TC center at lower levels (Xu and Takemi, 2022; Nicholls, 2015; Wing et al., 2016).

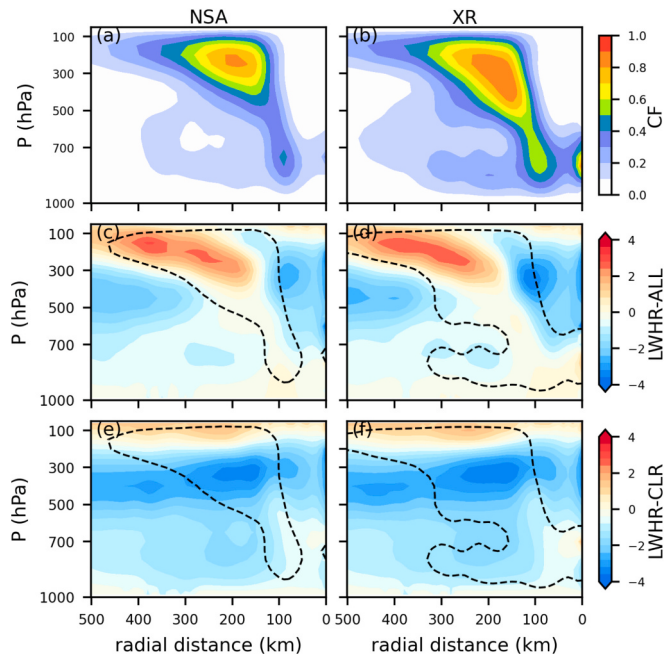


Fig. 7. WRF simulated vertical cross-sections of cloud fraction (a–b), the longwave radiative heating rate for the all-sky (LWHR-ALL; c–d) and clear-sky (LWHR-CLR; e–f), averaged in the southwestern quadrant for the period of 0000 UTC 23 July to 0000 UTC 25 July. In (c–f), the dashed line indicates the CF contour of 0.2 to facilitate the result interpretation. The degree of eyewall tilt, calculated as the difference between the eyewall cloud radii at 700 hPa and 150 hPa (Yang et al., 2022), is 30 km for the NSA simulation and 40 km for the XR simulation.

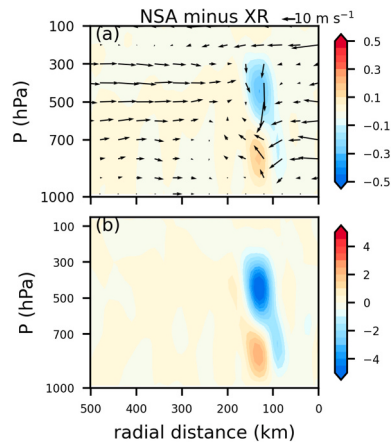


Fig. 8. WRF simulated differences (NSA minus XR) in vertical cross-sections of vertical velocity (a; shading; units: $m s^{-1}$), radial circulation (a; vectors; units: $m s^{-1}$) and latent heating rate (b; units: $K day^{-1}$), averaged in the southwestern quadrant for the period of 0000 UTC 23 July to 0000 UTC 25 July. In (a), the vertical wind speeds are timed by 200 to be comparable with the horizontal ones.

This overwhelms the instability effect and intensifies convections in the eyewall clouds in the NSA simulation (Fig. 10a), releasing more latent heat in the middle troposphere (Fig. 10b). This effect lowers the geopotential height in the eastern part of TC in the NSA simulation and shifts the TC track eastward.

5. Discussions

There are three relevant issues worthy of discussion. First, we have

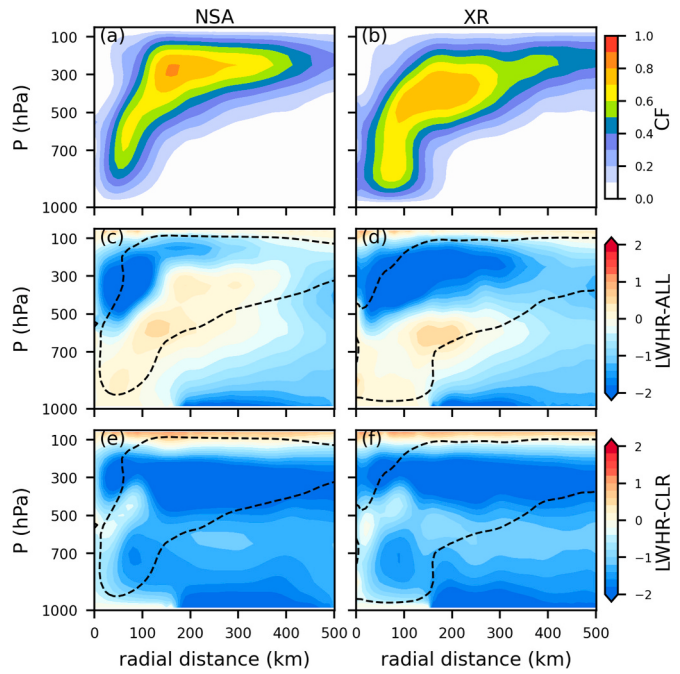


Fig. 9. Same as Fig. 7, but for the northeast quadrant of the period of 0000 UTC 25 July to 0000 UTC 26 July. The degree of eyewall tilt, calculated as the difference between the eyewall cloud radii at 700 hPa and 150 hPa (similar to the method from Yang et al., 2022), is 70 km for the NSA simulation and 150 km for the XR simulation.

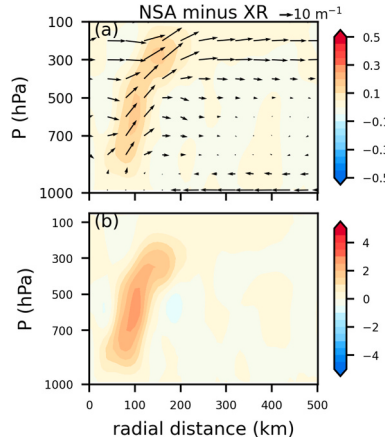


Fig. 10. Same as Fig. 8, but for the northeast quadrant of the period from 0000 UTC 25 July to 0000 UTC 26 July.

examined the sensitivity of the results to the choice of model horizontal resolution and cloud microphysical schemes. In additional sensitivity simulations, a finer resolution—3 km—was used in the inner domain. Those simulations indicate that the finer resolution reduces the bias in the TC track for both the NSA and XR simulations, diminishing the differences between them while keeping the NSA outcomes closer to the observations. Thus, we present results from the 9-km simulations in the previous sections to highlight the CVS effects. Regarding cloud microphysical schemes, we tested the WDM5 (Lim and Hong, 2010) and Morrison (Morrison et al., 2009) schemes, which did not cause much changes to the results.

Second, the TC intensity is also affected by the CVS, although its changes are less pronounced. In the pre-landfall phase, when the CVS difference in the western part dominates the changes of TC evolution, the TC intensity shows little difference between the two cases. This is

because the typhoon intensity (e.g., the maximum wind speed near the surface) is dominated by the eastern part of the TC. In contrast, in the landfall phase, when the NSA case has stronger convection in the eastern part, the NSA case clearly simulates stronger TC intensity than the XR case. Nevertheless, as the TC is in its decaying stage, the difference in TC intensity does not have sufficient time to become marked.

Third, we also examined SWCRE from the two simulations and found little difference between them. This indicates that the LWCRC plays a more important role in the TC evolution than the SWCRE, consistent with the findings of previous studies (Yang and Tan, 2020; Xu and Takemi, 2022). Thus, the SWCRE results are not presented above.

6. Conclusions

This study incorporated the NSA cloud-fraction scheme in the WRF Model to explore how CVS variations may influence the TC evolution, using the Typhoon In-Fa (2021) as a case study. Results show that using the NSA scheme yields larger/smaller IWP in the eastern/western part of the TC and smaller cloud fraction at most levels than using the conventional XR cloud-fraction scheme. In both the pre-landfall and landfall phases, the CVS differences cause the simulated TC track in the NSA simulation to shift eastward and get closer to the observations compared with that in the XR simulation. However, the underlying mechanisms differ between the two phases because of the TC asymmetric structure and phase evolution.

First, the NSA scheme consistently simulates smaller cloud fractions at most levels compared to the XR scheme on both the eastern and western parts of the TC. Consequently, the XR scheme tends to have stronger LWCRC, increasing the instability on both parts of the TC and invigorating the convection. Second, as the TC intensity is notably stronger in the eastern part (particularly in the northeast quadrant) than in the western part (especially the southwest quadrant), the northeast quadrant tends to have a horizontally distributed cloud layer. There, the NSA scheme simulates a more pronounced horizontal gradient of LWCRC, which amplifies the secondary circulation. During the pre-landfall phase, the effects of increased instability and enhanced secondary circulation in the northeast quadrant tend to counterbalance each other. Therefore, changes in the TC track are predominantly influenced by the instability effect in the southwest quadrant, where convective activities are enhanced in the XR simulation, shifting its TC track westward. However, during the landfall phase, cloud fraction decreases across the entire TC, diminishing the instability effect and allowing the secondary circulation effects in the northeast quadrant to become dominant. This causes stronger convective activities in the east of the TC in the NSA simulation, shifting the TC track eastward.

In summary, this study underscores the critical role of CVS in the development of TC. The CVS influences the vertical and horizontal cloud radiative heating rates, which can subsequently modulate the convective activities and thus impact the TC evolution. Note that In-Fa (2021) is a special individual case with a relatively larger outer size. The CVS effects on the TC development could be sensitive to the variations in TC intensity and size. Further studies are warranted to comprehensively assess the CVS effects in different TC cases.

CRediT authorship contribution statement

Enwang Luo: Writing – review & editing, Writing – original draft, Visualization, Validation, Supervision, Software, Resources, Project administration, Methodology, Investigation, Funding acquisition, Formal analysis, Data curation, Conceptualization. **Guoxing Chen:** Writing – review & editing, Writing – original draft, Visualization, Validation, Supervision, Software, Resources, Project administration, Methodology, Investigation, Funding acquisition, Formal analysis, Data curation, Conceptualization. **Wei-Chyung Wang:** Writing – review & editing, Writing – original draft. **Jie Feng:** Writing – review & editing, Writing – original draft. **Yanhong Gao:** Writing – review & editing,

Writing – original draft.

Declaration of competing interest

The authors declare no conflict of interest.

Data availability

The WRF used in this study can be obtained from https://www2.mmm.ucar.edu/wrf/users/download/get_source.html. The FNL data are available at the NCAR Research Data Archive (<https://rda.ucar.edu/datasets/ds083.2>). The JTWC best track data of TC are available at <https://www.metoc.navy.mil/jtvc/jtvc.html?best-tracks>.

Acknowledgments

This study is supported by the National Key Research and Development Program of China (2021YFC3000801) and the National Natural Science Foundation of China (42275074). The authors thank three anonymous reviewers for their insightful comments and suggestions, which greatly help improve the manuscript.

References

- Bu, Y.P., Fovell, R.G., Corbosiero, K.L., 2014. Influence of cloud-radiative forcing on tropical cyclone structure. *J. Atmos. Sci.* 71, 1644–1662. <https://doi.org/10.1175/JAS-D-13-0265.1>.
- Chen, G., Wang, W.C., 2016. Aerosol-stratocumulus-radiation interactions over the Southeast Pacific: Implications to the underlying air-sea coupling. *J. Atmos. Sci.* 73 (7), 2759–2771. <https://doi.org/10.1175/JAS-D-15-0277.1>.
- Chen, G., Yang, J., Bao, Q., Wang, W.-C., 2018. Intraseasonal responses of the East Asia summer rainfall to anthropogenic aerosol climate forcing. *Clim. Dyn.* 51 (11), 3985–3998. <https://doi.org/10.1007/s00382-017-3691-0>.
- Chen, G., Wang, W.-C., Cheng, C.-T., Hsu, H.-H., 2021. Extreme snow events along the coast of the Northeast United States: potential changes due to global warming. *J. Clim.* 34 (6), 2337–2353. <https://doi.org/10.1175/JCLI-D-20-0197.1>.
- Chen, G., Wang, W., Yang, S., Wang, Y., Zhang, F., Wu, K., 2023. A neural network-based scale-adaptive cloud-fraction scheme for GCMs. *J. Adv. Model. Earth Syst.* 15, e2022MS003415. <https://doi.org/10.1029/2022MS003415>.
- Craig, G., 1996. Numerical experiments on radiation and tropical cyclones. *Q. J. R. Meteorol. Soc.* 122, 415–422. <https://doi.org/10.1002/qj.49712253006>.
- DeHart, J.C., Houze, R.A., Rogers, R.F., 2014. Quadrant distribution of tropical cyclone inner-core kinematics in relation to environmental shear. *J. Atmos. Sci.* 71 (7), 2713–2732. <https://doi.org/10.1175/JAS-D-13-0298.1>.
- Dudhia, J., 1989. Numerical study of convection observed during the Winter Monsoon Experiment using a mesoscale two-dimensional model. *J. Atmos. Sci.* 46, 3077–3107. [https://doi.org/10.1175/1520-0469\(1989\)046<3077>2.0.CO;2](https://doi.org/10.1175/1520-0469(1989)046<3077>2.0.CO;2).
- Fovell, R.G., Bu, Y.P., Corbosiero, K.L., Tung, W.W., Cao, Y., Kuo, H.C., Su, H., 2016. Influence of cloud microphysics and radiation on tropical cyclone structure and motion. *Meteorol. Monogr.* 56, 11.1–11.27. <https://doi.org/10.1175/AMSMONOGRAPH-D-15-0006.1>.
- Fu, Q., Krueger, S.K., Liou, K.N., 1995. Interactions of radiation and convection in simulated tropical cloud clusters. *J. Atmos. Sci.* 52, 1310–1328. [https://doi.org/10.1175/1520-0469\(1995\)052-1310>2.0.CO;2](https://doi.org/10.1175/1520-0469(1995)052-1310>2.0.CO;2).
- Gray, W.M., Jacobson, R.W.J., 1977. Diurnal variation of deep cumulus convection. *Mon. Weather Rev.* 105, 1171–1188. [https://doi.org/10.1175/1520-0493\(1977\)105<1171>2.0.CO;2](https://doi.org/10.1175/1520-0493(1977)105<1171>2.0.CO;2).
- Hobgood, J.S., 1986. A possible mechanism for the diurnal oscillation of tropical cyclones. *J. Atmos. Sci.* 43, 2901–2922. [https://doi.org/10.1175/1520-0469\(1986\)043<2901>2.0.CO;2](https://doi.org/10.1175/1520-0469(1986)043<2901>2.0.CO;2).
- Hong, S.Y., Noh, Y., Dudhia, J., 2006. A new vertical diffusion package with an explicit treatment of entrainment processes. *Mon. Weather Rev.* 134, 2318–2341. <https://doi.org/10.1175/MWR3199.1>.
- Houze, R.A., 2010. Clouds in tropical cyclones. *Mon. Weather Rev.* 138, 293–344. <https://doi.org/10.1175/2009MWR2989.1>.
- Iacono, M.J., Delamere, J.S., Mlawer, E.J., Shephard, M.W., Clough, S.A., Collins, W.D., 2008. Radiative forcing by long-lived greenhouse gases: Calculations with the AER radiative transfer models. *J. Geophys. Res. Atmos.* 113 (D13). <https://doi.org/10.1029/2008JD009944>.
- Janjić, Z.I., 1994. The step-mountain eta coordinate model: further developments of the convection, viscous sublayer, and turbulence closure schemes. *Mon. Weather Rev.* 122 (5), 927–945. [https://doi.org/10.1175/1520-0493\(1994\)122%3C0927:TSMECM%3E2.0.CO;2](https://doi.org/10.1175/1520-0493(1994)122%3C0927:TSMECM%3E2.0.CO;2).
- Khain, A., Rosenfeld, D., Pokrovsky, A., 2005. Aerosol impact on the dynamics and microphysics of deep convective clouds. *Q. J. R. Meteorol. Soc.* 131 (611), 2639–2663. <https://doi.org/10.1256/qj.04.62>.
- Li, Y., Gao, Y., Chen, G., Wang, G., Zhang, M., 2024. Decomposition and reduction of WRF-modeled wintertime cold biases over the Tibetan Plateau. *Clim. Dyn.* 1–15. <https://doi.org/10.1007/s00382-024-07126-0>.

- Lim, K.S., Hong, S.Y., 2010. Development of an effective double-moment cloud microphysics scheme with prognostic cloud condensation nuclei (CCN) for weather and climate models. *Mon. Weather Rev.* 138 (5), 1587–1612. <https://doi.org/10.1175/2009MWR2968.1>.
- Miller, R.A., Frank, W.M., 1993. Radiative forcing of simulated tropical cloud clusters. *Mon. Weather Rev.* 121, 482–498. [https://doi.org/10.1175/1520-0493\(1993\)121<0482>2.0.CO;2](https://doi.org/10.1175/1520-0493(1993)121<0482>2.0.CO;2).
- Morrison, H., Thompson, G., Tatarskii, V., 2009. Impact of cloud microphysics on the development of trailing stratiform precipitation in a simulated squall line: Comparison of one- and two-moment schemes. *Mon. Weather Rev.* 137 (3), 991–1007. <https://doi.org/10.1175/2008MWR2556.1>.
- Muller, C.J., Romps, D.M., 2018. Acceleration of tropical cyclogenesis by self-aggregation feedbacks. *Proc. Natl. Acad. Sci. USA* 115 (12), 2930–2935. <https://doi.org/10.1073/pnas.1719967115>.
- Nicholls, M.E., 2015. An investigation of how radiation may cause accelerated rates of tropical cyclogenesis and diurnal cycles of convective activity. *Atmos. Chem. Phys.* 15, 9003–9029. <https://doi.org/10.5194/acp-15-9003-2015>.
- Nie, Y., Sun, J., 2022. Moisture sources and transport for extreme precipitation over Henan in July 2021. *Geophys. Res. Lett.* 49 (4), e2021GL097446. <https://doi.org/10.1029/2021GL097446>.
- Olfateh, M., Callaghan, D.P., Nielsen, P., Baldock, T.E., 2017. Tropical cyclone wind field asymmetry—Development and evaluation of a new parametric model. *J. Geophys. Res. Oceans* 122 (1), 458–469. <https://doi.org/10.1002/2016JC012237>.
- Reasor, P.D., Rogers, R., Lorsolo, S., 2013. Environmental flow impacts on tropical cyclone structure diagnosed from airborne Doppler radar composites. *Mon. Weather Rev.* 141 (9), 2949–2969. <https://doi.org/10.1175/MWR-D-12-00334.1>.
- Ruppert Jr., J.H., Wing, A.A., Tang, X., Duran, E.L., 2020. The critical role of cloud-infrared feedback in tropical cyclone development. *Proc. Natl. Acad. Sci. USA* 117, 27884–27892. <https://doi.org/10.1073/pnas.2013584117>.
- Seinfeld, J.H., Bretherton, C., Carslaw, K.S., Coe, H., DeMott, P.J., Dunlea, E.J., Wood, R., 2016. Improving our fundamental understanding of the role of aerosol–cloud interactions in the climate system. *Proc. Natl. Acad. Sci. USA* 113 (21), 5781–5790. <https://doi.org/10.1073/pnas.1514043113>.
- Song, Y., Chen, G., Wang, W.-C., 2019. Aerosol direct radiative and cloud adjustment effects on surface climate over eastern China: analyses of WRF model simulations. *J. Clim.* 32 (4), 1293–1306. <https://doi.org/10.1175/jcli-d-18-0236.1>.
- Sundqvist, H., Berge, E., Kristjánsson, J.E., 1989. Condensation and cloud parameterization studies with a mesoscale numerical weather prediction model. *Mon. Weather Rev.* 117, 1641–1657. [https://doi.org/10.1175/1520-0493\(1989\)117<1641>2.0.co;2](https://doi.org/10.1175/1520-0493(1989)117<1641>2.0.co;2).
- Tang, X., Cai, Q., Fang, J., et al., 2019. Land-sea contrast in the diurnal variation of precipitation from landfalling tropical cyclones. *J. Geophys. Res. Atmos.* 124 (22), 12010–12021. <https://doi.org/10.1029/2019JD031454>.
- Tao, W.-K., Simpson, J., Lang, S., Sui, C.-H., Ferrier, B., Chou, M.-D., 1996. Mechanisms of cloud-radiation interaction in the tropics and midlatitudes. *J. Atmos. Sci.* 53, 2624–2651. [https://doi.org/10.1175/1520-0469\(1996\)053<2624>2.0.CO;2](https://doi.org/10.1175/1520-0469(1996)053<2624>2.0.CO;2).
- Thompson, G., Rasmussen, R.M., Manning, K., 2004. Explicit forecasts of winter precipitation using an improved bulk microphysics scheme. Part I: Description and sensitivity analysis. *Mon. Weather Rev.* 132 (2), 519–542. [https://doi.org/10.1175/1520-0493\(2004\)132<0519>2.0.CO;2](https://doi.org/10.1175/1520-0493(2004)132<0519>2.0.CO;2).
- Tiedtke, M., 1989. A comprehensive mass flux scheme for cumulus parameterization in large-scale models. *Mon. Weather Rev.* 117 (8), 1779–1800. [https://doi.org/10.1175/1520-0493\(1989\)117<1779>2.0.CO;2](https://doi.org/10.1175/1520-0493(1989)117<1779>2.0.CO;2).
- Ueno, M., 2007. Observational analysis and numerical evaluation of the effects of vertical wind shear on the rainfall asymmetry in the typhoon inner-core region. *J. Meteorol. Soc. Jpn. Ser. II* 85 (2), 115–136. <https://doi.org/10.2151/jmsj.85.115>.
- Wang, X., Liu, Y., Bao, Q., Wu, G., 2015. Comparisons of GCM cloud cover parameterizations with cloud-resolving model explicit simulations. *Sci. China Earth Sci.* 58 (4), 604–614. <https://doi.org/10.1007/s11430-014-4989-y>.
- Wang, X., Miao, H., Liu, Y., Bao, Q., He, B., Li, J., Zhao, Y., 2022. The use of satellite data-based “critical relative humidity” in cloud parameterization and its role in modulating cloud feedback. *J. Adv. Model. Earth Syst.* 14 (10), e2022MS003213. <https://doi.org/10.1029/2022MS003213>.
- Wang, Y., Yang, S., Chen, G., Bao, Q., Li, J., 2023. Evaluating two diagnostic schemes of cloud-fraction parameterization using the CloudSat data. *Atmos. Res.* 282, 106510. <https://doi.org/10.1016/j.atmosres.2022.106510>.
- Webster, P.J., Stephens, G.L., 1980. Tropical upper-tropospheric extended clouds: Inference from winter MONEX. *J. Atmos. Sci.* 37, 1521–1541. [https://doi.org/10.1175/1520-0469\(1980\)037<1521>2.0.CO;2](https://doi.org/10.1175/1520-0469(1980)037<1521>2.0.CO;2).
- Wen, G., Huang, G., Huang, H., Liu, C., Bi, X., 2019. Observed rainfall asymmetry of tropical cyclone in the process of making landfall in Guangdong, South China. *Int. J. Climatol.* 39 (7), 3379–3395. <https://doi.org/10.1002/joc.6027>.
- Wing, A.A., Camargo, S.J., Sobel, A.H., 2016. Role of radiative-convective feedbacks in spontaneous tropical cyclogenesis in idealized numerical simulations. *J. Atmos. Sci.* 73, 2633–2642. <https://doi.org/10.1175/JAS-D-15-0380.1>.
- Wu, L., Wang, B., 2000. A potential vorticity tendency diagnostic approach for tropical cyclone motion. *Mon. Weather Rev.* 128, 1899–1911. [https://doi.org/10.1175/1520-0493\(2000\)128<1899:APVTD>2.0.CO;2](https://doi.org/10.1175/1520-0493(2000)128<1899:APVTD>2.0.CO;2).
- Wu, Z., Zhang, Y., Zhang, L., Zheng, H., Huang, X., 2022. A comparison of convective and stratiform precipitation microphysics of the record-breaking Typhoon In-Fa (2021). *Remote Sens.* 14 (2), 344. <https://doi.org/10.3390/rs14020344>.
- Xu, K.-M., Randall, D.A., 1995. Impact of interactive radiative transfer on the macroscopic behavior of cumulus ensembles. Part II: Mechanisms for cloud-radiation interactions. *J. Atmos. Sci.* 52, 800–817. [https://doi.org/10.1175/1520-0469\(1995\)052<0800>2.0.CO;2](https://doi.org/10.1175/1520-0469(1995)052<0800>2.0.CO;2).
- Xu, K.-M., Randall, D.A., 1996. A semiempirical cloudiness parameterization for use in climate models. *J. Atmos. Sci.* 53 (21), 3084–3102. [https://doi.org/10.1175/1520-0469\(1996\)053<3084>2.0.co;2](https://doi.org/10.1175/1520-0469(1996)053<3084>2.0.co;2).
- Xu, M., Takemi, T., 2022. Radiative effects on tropical cyclone development in different life stages. *Mon. Weather Rev.* 150 (12), 3131–3150. <https://doi.org/10.1175/MWR-D-21-0337.1>.
- Yang, B., Tan, Z.-M., 2020. Interactive radiation accelerates the intensification of the midlevel vortex for tropical cyclogenesis. *J. Atmos. Sci.* 77, 4051–4065. <https://doi.org/10.1175/JAS-D-20-0094.1>.
- Yang, J., Wang, W.-C., Chen, G., Bao, Q., Qi, X., Zhou, S., 2018. Intraseasonal variation of the black carbon aerosol concentration and its impact on atmospheric circulation over the southeastern Tibetan Plateau. *J. Geophys. Res. Atmos.* 123 (19), 10881–10894. <https://doi.org/10.1029/2018JD029013>.
- Yang, B., Nie, J., Tan, Z., 2021. Radiation feedback accelerates the formation of Typhoon Haiyan (2013): the critical role of mid-level circulation. *Geophys. Res. Lett.* 48. <https://doi.org/10.1029/2021GL094168>.
- Yang, B., Guo, X., Gu, J., Nie, J., 2022. Cloud-radiation feedback prevents tropical cyclones from reaching higher intensities. *Geophys. Res. Lett.* 49. <https://doi.org/10.1029/2022GL100067>.
- Zhang, C., Wang, Y., Hamilton, K., 2011. Improved representation of boundary layer clouds over the Southeast Pacific in ARW-WRF using a modified Tiedtke cumulus parameterization scheme. *Mon. Weather Rev.* 139 (11), 3489–3513. <https://doi.org/10.1175/MWR-D-10-05091.1>.